ACS OMEGA

Open Access

http://pubs.acs.org/journal/acsodf

Article

Synthesis and Local Characterization of CoO Nanoparticles in Distinct Phases: Unveiling Polymorphic Structures

Suzilene V. Santos, Cleidilane S. Costa, Waldeci Paraguassu, Crystian W. C. Silva, Larissa Otubo, Katiusse S. Souza, Bruno S. Correa, Arnaldo A. Miranda-Filho, Wanderson L. Ferreira, Artur W. Carbonari,* and Gabriel A. Cabrera-Pasca*

Cite This: *ACS Omega* 2024, 9, 42883−42894

Read Online

ACCESS | Metrics & More | Article Recommendations

ABSTRACT: The advancement of functional nanomaterials has become a major focus of recent research, driven by the exceptional properties these materials display compared to their macroscopic (bulk) counterparts. Cobalt oxide nanoparticles (CoO-NPs) stand out primarily for their catalytic and magnetic properties, which can enable a range of technological applications, such as advanced catalysts, drug delivery systems, implants, prosthetics, sensors. However, in addition to the dependence on factors such as size, morphology, and functionalization, the properties of CoO-NPs are significantly influenced by the crystal structure. Therefore, local investigation into the polymorphic structures of CoO at the nanometric scale may provide new insights into the local structural and magnetic characteristics of these systems. In this report, we address the synthesis and local characterization of cobalt oxide (CoO) nanoparticles in the rock-salt cubic fcc-CoO and Wurtzite hpc-CoO phases, obtained through thermal decomposition. We analyze the influence of oleylamine and oleic acid ligands on the structural and morphological control of these systems. The obtained nanoparticles were characterized using conventional techniques such as X-ray diffraction (XRD), transmission electron microscopy, Raman spectroscopy, and Fourier-transform infrared spectroscopy. Local characterization was carried out by the perturbed angular correlation (PAC) nuclear technique using the radioactive tracer ^{111}In(^{111}Cd). Measurements were conducted at 295 and 10 K to investigate possible magnetic phase transitions in these systems. XRD results confirmed the formation of fcc-CoO and hcp-CoO phases. The phase fcc was obtained with the pair of oleylamine and oleic acid ligands, while the phase hcp phase was synthesized using only oleylamine. Additionally, nanoparticles synthesized with oleylamine and oleic acid exhibited better morphological control compared to those produced with only oleylamine. Raman spectroscopy analyses suggest a phase transformation process resulting in Co_3O_4. PAC results for hyperfine interactions at the ^{111}In(^{111}Cd) probe nucleus, indicate that the hcp-CoO phase shows smaller hyperfine magnetic interactions (B_{hf} = 1 T) compared to the fcc-CoO phase (B_{hf} = 17 T). This suggests the mechanism of superexchange interactions, which are strongly influenced by the Co−O−Co bond angle, which is 110° for the hpc-CoO phase and 180° for the fcc-CoO phase due to the geometries of the systems.

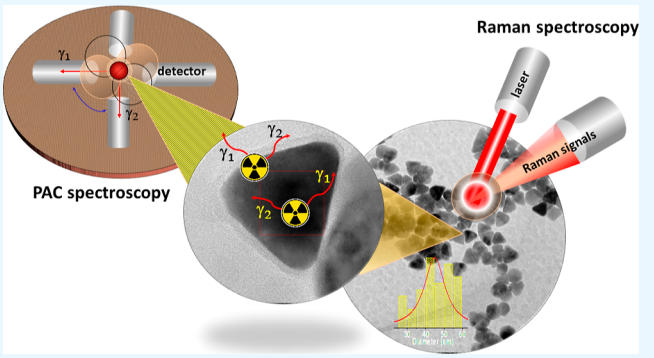

INTRODUCTION

In recent years, an enormous amount of effort has been focused on developing procedures for the synthesis of nanostructured materials. Among all of these methods, the bottom-up synthesis strategy has received substantial attention from the scientific community because of its ability to allow controlled synthesis of nanomaterials. In contrast to bulk-type macrometric objects, this technique allows for exact control over many characteristics such as size, shape, composition, and structural order, among others.[1,2] All of which have a direct impact on the intrinsic physicochemical characteristics of nanometric objects. Nanoparticle (NPs) science and related technologies have enabled important advances in a variety of areas, including nanomedicine, engineering, and agriculture, among others. These technological advances have led the way to the development of novel sensors, actuators, carriers, and other devices, resulting in the creation of novel drugs, ultraresponsive diagnostics, implants, and prostheses, as well as improved drug delivery systems and vaccines.[3,4]

Received: June 5, 2024
Revised: September 27, 2024
Accepted: October 4, 2024
Published: October 10, 2024

At the nanoscale, a substantial portion of the atoms present in the system are on or near the surface, resulting in intriguing processes that are currently being studied extensively. For example, the origin of ferromagnetic behavior in nanoscale materials, which typically exhibit paramagnetic behavior, remains an open question. Some researchers believe this unusual magnetism is due to surface effects and that bulk defects (such as vacancies) can cause uncompensated spins, resulting in a ferromagnetic response.[4,5] Another topic of research in nanoscale systems is the stability of crystalline phases, which are rarely stable at larger sizes, resulting in new chemical−physical properties such as ferromagnetic-like responses.[6,7]

Particularly, cobalt oxide nanoparticles (Co-NPs), including rock-salt-CoO, Wurtzite-CoO, zincblend-CoO, and cobaltite (Co_3O_4), which corresponds to the cubic spinel phase of the Co oxide, have sparked significant interest due to their widespread applications in a variety of industrial sectors, including rechargeable lithium batteries,[8] catalysts,[9] gas sensors,[10] and biomedicine.[11] This broad range of applications is attributed to the different magnetic, mechanical, optical, chemical, and electrical properties exhibited by the crystallographic phases of cobalt oxide when reduced to the nanoscale.[12]

The polymorphism of the CoO-NPs, resulting in different crystalline structures, depends on the synthesis route and the reduction atmosphere, owing to the different oxidation states of cobalt. Particularly, the fcc-CoO rocksalt structure remains thermodynamically stable, while the hcp-CoO structure is relatively unstable and can be easily transformed into a cubic structure by application of heat and pressure.[13]

The development of functionalized CoO-NPs with well-defined structure and morphology is of particular interest for various applications. For instance, in catalytic applications (such as oxidation, hydrogenation, and hydroamination reactions), the functionalization of the nanoparticle surface is crucial. Specifically, this occurs because the adsorbed ligands on the surface act as mediators, facilitating the interaction between the nanoparticle and its surroundings. This characteristic enables the manipulation of not only the hydrophilicity of the nanoparticles, the thermal stability, and mechanical resistance but also their electronic properties. This interaction can influence the electronic properties not only of the direct interaction sites (ligand-surface), but also of adjacent sites, allowing fine-tuning of properties related to the activity and selectivity of the catalyst.[14] Another interesting aspect is the role of surface functionalization in governing the morphology of CoO nanostructures and its subsequent impact on the applications of these systems. For example, Cai et al. successfully synthesized interconnected 2D CoO nanosheets, which, after thermal treatment, were transformed into Co_3O_4 while maintaining their original morphology. From this perspective, the significant catalytic activity of the Co_3O_4 spinel phase, coupled with the 2D morphology of the system, enabled the presence of numerous active sites of $Co^{3+}$and O_2 on the surface. This configuration contributed to the material's exceptional catalytic performance.[15] Thus, the customization of these fundamental aspects for CoO nanoparticles can be adjusted using chemical protocols by varying parameters such as precursor concentration, reaction temperature, reaction time, and the type of ligands used, with oleic acid and oleylamine being frequently reported in the literature.[16,17]

For example, according to previous studies realized by He et al., hpc-CoO NPs can be obtained by the thermal decomposition method at 220 °C for 1 h, using cobalt salts and oleylamine, as a reducer and surfactant.[18] Ravindra et al. stated that hpc-CoO NPs were formed by thermolysis at 296 °C, under mechanical stirring.[13] Meanwhile, Deori and Deka reported that fcc-CoO NPs were created by solvothermal-driven chemical processes at a temperature of 220 °C.[19] some studies are available in the literature, aspects related to the formation mechanism, as well as the physical and chemical properties of hpc-CoO nanoparticles, remain challenging and largely unexplored due to their phase instability.

Therefore, a localized study of these systems using experimental nuclear techniques is crucial as they provide detailed information at the atomic scale in nanoparticles. This local information can be correlated with results obtained through other techniques such as X-ray diffraction, Raman spectroscopy, and transmission electron microscopy (TEM). This allows for a comprehensive understanding of the systems. This set of information allows for excellent characterization in terms of crystalline structure, stoichiometry, and crystalline and magnetic phase transitions that occur in the vicinity of surfaces or interfaces of the nanomaterials.[20,21]

Among nuclear techniques, nuclear magnetic resonance (NMR), Mössbauer spectroscopy, and perturbed angular correlation (PAC) stand out. The PAC technique is particularly notable as a nonresonant nuclear method, making it especially useful for local structural and magnetic characterization over a wide range of temperatures[22,23] This technique measures the angular distribution of gamma photons emitted by a radioactive probe nucleus, allowing for detailed local characterization of the material properties. The precision of this spectroscopic technique arises from the hyperfine interactions between suitable probe nuclei and their near environments into samples. These interactions provide valuable information on the local electric field and the magnetic environment surrounding the probe, which contributes to a deeper understanding of the material characteristics.[24]

The angular distribution pattern extracted from a PAC experiment is usually expressed in terms of hyperfine parameters, such as the magnetic interaction frequency (ν_M), the electric quadrupole frequency (ν_Q) and the asymmetry parameter (η). Since the PAC technique needs the presence of radioactive atoms inside the nanoparticle which can be difficult to produce through implantation processes, its application in the re- search of nanoparticles is still relatively unexplored. However, if the radionuclides utilized in the PAC technique are added during the nucleation and growth processes of nanomaterials, this limitation can be circumvented. This allows for atomic-level investigation of several particle regions, including the coating, interface, and core of the nanoparticles. For example, the PAC technique has been applied recently to further understand the size influence on magnetism in CoO-NPs[25] and to investigate the impact of ligand pairs in the synthesis and stabilization of Fe_3O_4 nanoparticles.[21] Furthermore, because PAC is a local method, it allows the mapping of vacancies and crystal structural distortions surrounding a specific site occupied by probe.[25,26]

In this report, we address the synthesis and local characterization of cobalt oxide (CoO) nanoparticles in the fcc and hcp phases, obtained through thermal decomposition. To obtain nanoparticles with precise dimensions and morphology, we rigorously controlled the process parameters,

https://doi.org/10.1021/acsomega.4c05308
ACS Omega 2024, 9, 42883−42894

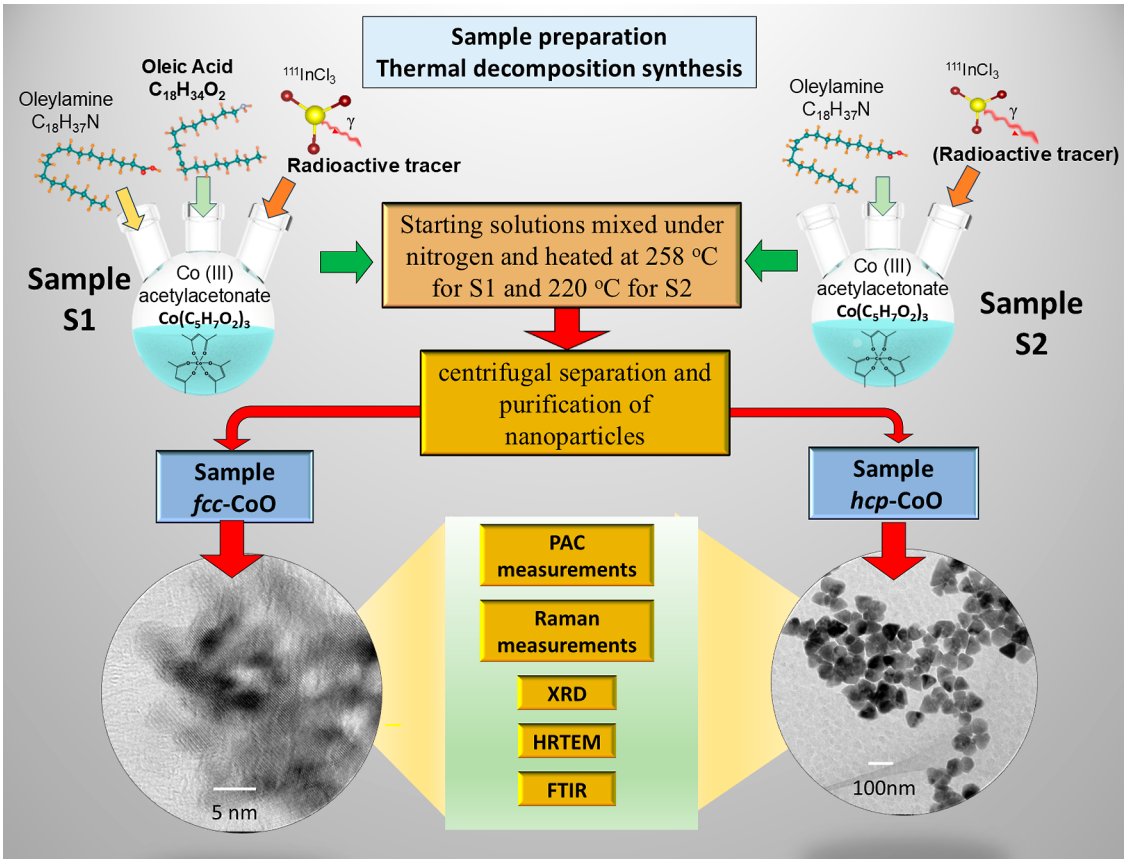

Figure 1. Schematic illustration showing the steps involved in the preparation and characterization of fcc-CoO (S_1) and hcp-CoO (S_2) nanoparticles, highlighting the synthesis conditions and reagents used. In the context of characterization techniques, local PAC analysis and Raman spectroscopy are emphasized, along with other techniques used such as XRD, HRTEM, and FTIR.

including the choice of chemicals, nucleation temperature, growth time, and reaction time. For local characterization, we used the PAC technique using the radioactive tracer ^{111}In-(^{111}Cd), with measurements conducted at 295 and 10 K to investigate possible magnetic phase transitions in these systems. In addition, we used Raman spectroscopy to assess the structural stability of the nanoparticles. The data obtained from these spectroscopic techniques were correlated with structural and morphological information obtained by TEM (TEM/HRTEM), X-ray diffraction (XRD), and Fourier-transform infrared spectroscopy (FTIR). This integrated approach enabled a detailed understanding of the nanoparticle properties and their correlation with the observed physical characteristics.

EXPERIMENTAL SECTION

Synthesis of Fcc-CoO and Hcp-CoO. Cobalt(III) acetylacetonate ($Co(acac)_3$) was used as the metal precursor in the synthesis of cobalt oxide nanoparticles, together with varying quantities of oleylamine ($C_{18}H_{37}N$) and oleic acid ($C_{18}H_{34}O_2$). The reagents were placed into a flask with three necks as part of the synthesis process. To promote heat exchange between the equipment and the container, the reaction flask was set atop a heating mantle that was covered with aluminum foil. To monitor the internal temperature of the flask while it was being heated, a thermocouple was placed inside. Furthermore, a cold water flow was utilized in an Allihn condenser to avoid stoichiometric losses during the synthesis. Additionally, a connection for the flow of nitrogen was included, which provided an inert atmosphere for the synthesis.

Carefully controlled experimental conditions were employed to ensure the synthesis of cobalt oxide nanoparticles with the intended size and shape. Oleic acid and oleylamine may have a significant impact on crystal orientation, size control, and nanoparticle stabilization. The samples underwent a variety of steps and conditions during the synthesis process. Following a heating stage at a rate of 6 °C per minute until reaching the nucleation temperature of 130 °C for 10 min, the temperature was increased to certain values for each synthesized sample and held for defined reaction times. For a sample named S_1, oleylamine, oleic acid, and $Co(acac)_3$ were used as reagents. Sample S_1 underwent a reaction lasting 1 h at an average temperature of 270 °C. Similarly, the other sample, named S_2, was synthesized by reacting only oleylamine and $Co(acac)_3$ for 3 h at 220 °C.

After synthesis, the resulting solution was cooled and dissolved in various solvents, such as ethyl alcohol, toluene, and methyl ethyl ketone. These solvents were carefully selected to aid in the mixing and dissolution of the compounds present in the sample. To ensure complete mixing, the solution was then cleaned with an ultrasonic device. The nanoparticles were then separated from the solvent and any other potential contaminants using centrifugation. Samples synthesized with each solvent were subjected to centrifugation for 20 min at a speed of 10,000 rpm. Finally, the samples were vacuum-dried using a desiccator and a vacuum pump, reaching a pressure of up to 10^{-3} bar.

https://doi.org/10.1021/acsomega.4c05308
ACS Omega 2024, 9, 42883−42894

After drying, a pure powder was obtained and the characteristics of the samples were analyzed. (1) For both measurements, TEM and high-resolution transmission electron microscopy (HRTEM), samples were prepared by depositing a portion of a nanoparticle suspension solution in isopropanol alcohol onto a grid coated with Formvar and carbon. The powdered samples were prepared by dispersing them in isopropanol in an ultrasonic bath, then pouring them onto a copper grid covered with collodion film, and allowing them to air-dry. The Jeol-JEM 2100 transmission electron microscope, operating at an acceleration voltage of 200 kV and available at the Laboratory of Microscopy and Microanalysis (LMM) of the Center for Science and Technology of Materials at the Nuclear and Energy Research Institute (CECTM/IPEN), was used to measure the size distribution and morphology of samples S_1 and S_2. The images were captured at various magnifications to assess the shape and size distribution of the sample.

(2) The crystalline structure was determined using XRD performed with a Rigaku SmarLab model equipped with a high-resolution 2D HPAD detector located at the Research Reactor Center (CERPq/IPEN). Cu Kα radiation (λ = 1.54056 Å) was used to collect data in an angular range of 20−80° at 40 kV and 40 mA, with a step size of 0.01°.

(3) Fourier transform infrared spectroscopy (FTIR) measurements were taken after the synthesis of the fcc-CoO and hcp -CoO to characterize the coating materials that involve them. The oleic acid and oleylamine included in the coating layer of the NPs can be identified through FTIR measurements. Infrared spectra were obtained using the Bruker VERTEX 70v spectrometer with a spectral resolution of 4 cm^{-1} from the UFPA high pressure and vibrational spectroscopy laboratory. Measurements were carried out between 500 and 4000 cm^{-1} with attenuated total reflectance (ATR). Additionally, (4) the Micro Raman spectrometer (Jobin Yvon-T64000) was used at the UFPA vibrational spectroscopy and high pressure laboratory to analyze the samples employing Raman spectroscopy. Using the Fityk fitting tool, the Lorentzian function was used to fit the active Raman modes.

For atomic scale characterization, (5) PAC spectroscopy experiments were carried out in the Laboratory of Hyperfine Interactions at CERPq/IPEN in São Paulo, Brazil, using a spectrometer equipped with four BaF_2 detectors. In the preparation of the NP samples for the PAC measurements, specifically, 5 μL of radioactive $InCl_3$ with an activity of 20 μCi was added during synthesis. The highest number of impurity atoms estimated from this action is around 2.5×10^{11}. The precise concentration, however, is dependent on the diffusion of probe nuclei inside the sample and, consequently, on variables including reaction time, temperature, and ligand type. As a result, the final concentration cannot be measured; nonetheless, the estimate is approximately 100 ppb, which is insignificant enough to affect the sample characteristics.

All these characterizations along with the synthesis of samples are shown schematically in Figure 1.

PAC spectroscopy is based on the observation of hyperfine interactions between nuclear moments and extra-nuclear magnetic fields (B_{hf}) or with an electric field gradient (EFG). Details on the PAC measures and a description of the methodology can be found elsewhere.[23,27]

A model accounting for the fractional site populations (f) was used to fit the time-dependent anisotropy ratio function obtained from the experiments. This model is given by

$$R(t) = A_{22}G_{22}(t) = A_{22}\sum_i f_i G_{22}^i(t) \quad (1)$$

where A_{22} is the unperturbed angular correlation coefficient, and the perturbation factor $G_{22}(t)$ provides specific information about the hyperfine interactions.

For magnetic interactions, $G_{22}(t) = 0.2 + 0.4\cos(\omega_L t) + 0.4\cos(2\omega_L t)$, where $\omega_L = \mu_N g B_{hf}/\hbar$ is the Larmor frequency (note that $\nu_m = \omega_L/2\pi$), μ_N is the nuclear magneton and g is the nuclear g-factor. Thus, it is possible to determine the magnetic hyperfine field (B_{hf}) from the Larmor frequency extracted from measurements of $G_{22}(t)$.[28]

$G_{22}(t) = S_{20} + \sum_{n=1}^{3} S_{2n}(\eta)\cos(\omega_n t)$ represents the perturbation function for electric quadrupole interactions. The transition frequencies ω_n are related to the quadrupole frequency $\nu_Q = (eQV_{zz})/h$ through the relationship $\omega_n = g_n(\eta)\nu_Q$. These transition frequencies, as well as $S_{2n}(\eta)$ and $g_n(\eta)$ are known to be functions of the asymmetry parameter (η). The asymmetry parameter is defined as $\eta = (V_{xx} - V_{yy})/V_{zz}$ and is dependent on the diagonal components of the EFG tensor, V_{kk}, under the assumption that $|V_{xx}| \leq |V_{yy}| \leq |V_{zz}|$. Lastly, Q is the electric quadrupole moment of the probe nuclei. For both quadrupole electric and dipole magnetic static interactions, the width of the frequency distribution is given by a Lorentz broadening, which is parametrized by $\delta\omega$ exponential factor.

Given the well-known Q of the probe nucleus, the major component (V_{zz}) of the EFG can be calculated through the experimental determination of ν_Q. Additionally, the measure of η offers information on the configuration of the EFG in the crystallographic site where the probe nuclei are located. The local distortion of the crystallographic site causes a variation in the local charge distribution from axial symmetry, which is measured by the parameter η, which has a range of values from 0 to 1. It is important to emphasize that η provides information on the local symmetry surrounding the probe nucleus.

RESULTS AND DISCUSSION

Structural Characterization. The diffraction patterns of samples S_1 and S_2, as shown in Figure 1, reveal distinct crystal structures. For sample S_1, the peaks corresponding to the crystalline planes (111), (200), (220), (311) and (222) indicate a cubic crystal structure of the rocksalt (fcc-CoO), with lattice parameters of $a = b = c = 4.2500$ Å. The mean crystallite size, estimated using the Scherrer equation, is approximately 7 nm. In contrast, sample S_2 exhibits peaks corresponding to the (1 0 0), (0 0 2), (1 0 1), (1 0 2), (1 1 0), (1 0 3), (2 0 0), (1 1 2), and (2 0 1) planes, characteristic of a closed-packed hexagonal structure of cobalt monoxide (hcp-CoO), also known as Wurtzite. The lattice parameters obtained from the Rietveld refinement are $a = b = 3.2100$ and $c = 5.2400$ Å, consistent with the values in the literature.[18] The mean crystallite size, of S_2 sample, determined using the Scherrer equation, is approximately 28 nm.

In particular, the absence of additional phases, such as Co_3O_4 spinel types, was confirmed by Rietveld refinement for both samples, indicating the pure fcc structure for S_1 and the pure hcp structure for sample S_2. The X-ray diffraction patterns presented in Figure 2 represent the distinct crystallographic phases observed for S_1 and S_2, with the red curve representing the Rietveld refinement.

These results indicate that rigorous control of parameters such as ligand proportion, temperature, and growth time is

https://doi.org/10.1021/acsomega.4c05308
ACS Omega 2024, 9, 42883−42894

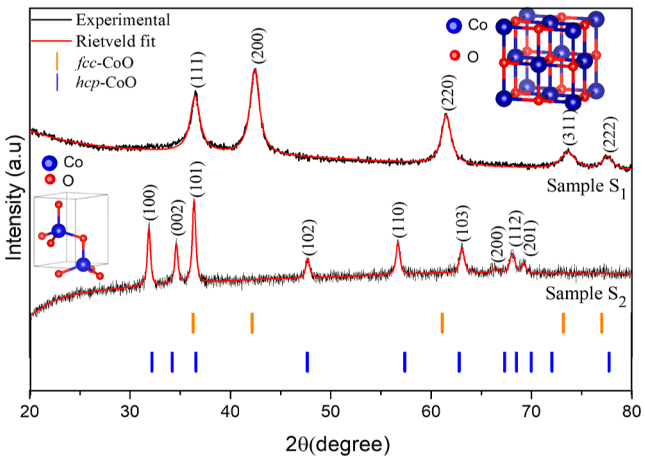

Figure 2. X-ray diffraction patterns of samples S_1 and S_2. The fcc-CoO was determined for sample S_1 whereas the hcp-CoO was obtained for the sample S_2. The red curve represents the fit obtained using the Rietveld method, indicating the absence of secondary phases in the samples.

crucial for obtaining pure phase CoO nanoparticles, as observed in recent studies.[16] Notably, the hcp-CoO phase, due to its metastable nature, has been frequently reported as challenging to stabilize and is prone to transition to the Co_3O_4 phase at temperatures above 200 °C.[29] In applications involving these systems, structural characteristics such as crystal orientation, crystallite size, and surface defects are crucial, especially in relation to their catalytic and magnetic properties. For instance, crystal orientation is essential for utilizing these systems as supports for the oriented growth of other nanostructures, such as $CoFe_2O_4$, and for optimizing gas selectivity in catalytic processes.[14,30,31] Additionally, factors such as crystallite size and surface defects significantly influence the magnetization properties of CoO nanoparticles.[15,25,32] On the other hand, from the perspective of nanoparticles, these characteristics are significantly related to the morphology.[19,33]

TEM and high-resolution transmission electron microscopy (HRTEM) were used to investigate the morphology of the samples (Figure 3). For sample S_1 the results indicate the formation of nanoclusters of a size of around 40 nm, resulting from the agglomeration of nanoparticles with an average size of 5 nm and a standard deviation σ = 1.6 nm (Figure 3a,b). The HRTEM image shown in Figure 3c reveals interplanar distances of 0.21 and 0.24 nm corresponding, respectively, to the planes (111) and (002) of fcc-CoO, along the [−110] zone axis as shown in Figure 3d.

The images in Figure 4 demonstrate aspects related to size, morphology, and structure for sample S_2. To investigate the average particle size, a histogram (inset of Figure 4a) was constructed showing nanoparticles with an estimated average size of 43 nm, with a standard deviation σ = 9.3 nm. This result, compared to the average crystallite size of 28 nm obtained by using the Scherrer equation, suggests that a single particle is composed of an assemblage of crystalline domains. Figure 4b illustrates the formation of nanoparticles with different morphologies, including triangular, circular, and hexagonal shapes. These morphological variations may be attributed to the surface (or plane) on which the surfactants are absorbed to stabilize the nanoparticles during the growth stage. The presence of surfactants on the nanoparticle surface is evidenced in Figure 4c, where an organic layer with a thickness of approximately 3 nm can be observed coating the particles. Our observation is in agreement with the research conducted by Jang et al., which suggests that the chemical stabilization of the surface facets is related to OH groups due to the remnant presence of organic material.[34] The HRTEM image shown in Figure 4e reveals interplanar distances of 0.25 and 0.50 nm attributed to the (002) and (001) planes of hcp-CoO, along the [110] zone axis as indexed in the FFT presented in Figure 4f, which is consistent with the lattice constant of the hcp-CoO structure.

These findings reveal significant differences in the structure, morphology, and size of samples S_1 (fcc-CoO) and S_2 (hcp-CoO). These differences indicate that the synthesis conditions such as temperature, chemical concentration, and reaction time strongly influence nanoparticle formation. These synthesis characteristics, which control the size, shape, and structure of nanoparticles, are essential to the kinetics of the nucleation reaction. For example, in fcc-CoO nanoparticles, smaller

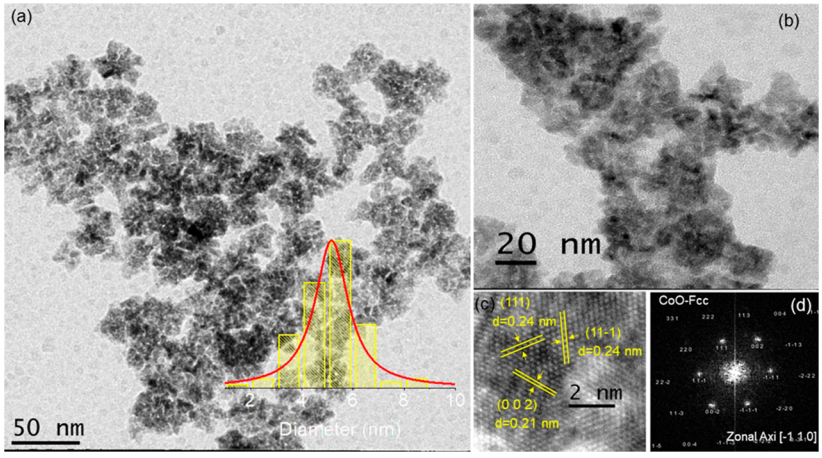

Figure 3. Images of sample S_1 observed by TEM/HRTEM are presented. (a) The image shows the morphology and size distribution of nanoparticles. (b) Higher magnification micrograph. (c) High-resolution image (HRTEM) displaying the interplanar distance corresponding to the (111) and (002) planes of fcc-CoO. (d) FFT obtained for the high-resolution image, showing the fcc-CoO planes indexed along the [−110] zone axis.

https://doi.org/10.1021/acsomega.4c05308
ACS Omega 2024, 9, 42883−42894

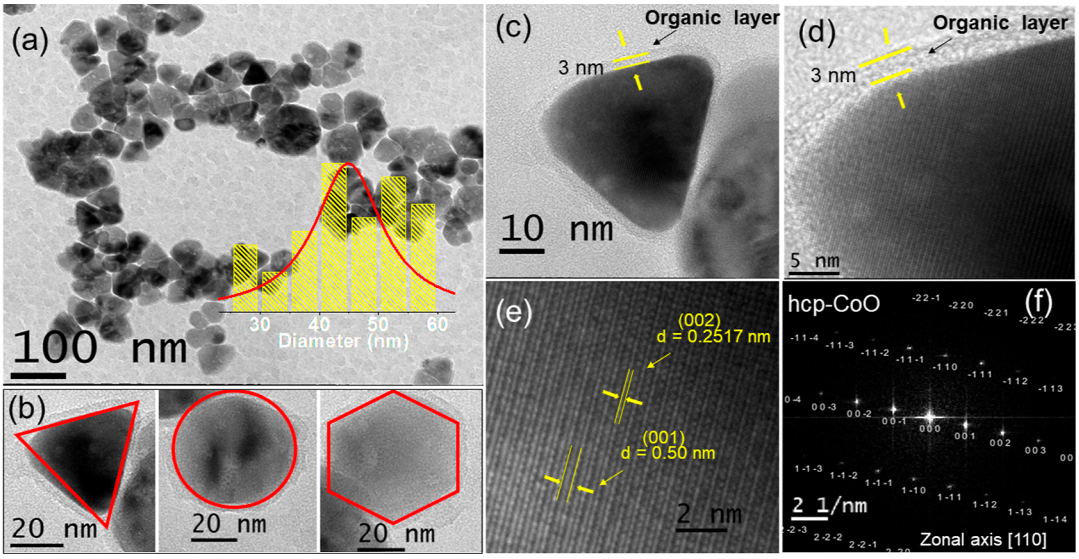

Figure 4. Images of sample S_2 observed by TEM are presented. (a) Micrograph of the nanoparticles and their size distribution (inset). (b) Nanoparticle morphology. (c,d) Nanoparticles at different magnifications, highlighting the organic coating. (e) HRTEM showing the (001) and (002) planes of hcp-CoO and their respective interplanar distances. (f) FFT obtained for the high-resolution image, showing the hcp-CoO planes indexed along the [110] zone axis.

particles are formed when the nucleation rate exceeds the growth rate. In contrast, bigger nanoparticles, such as hcp-CoO NPs, may develop if the growth rate exceeds the nucleation rate.[35,36]

Coating Characterization: FTIR. FTIR measurements are useful for characterizing the coating material of NPs, such as oleylamine and oleic acid for fcc-CoO and oleylamine for hcp-CoO NPs. Figure 5 shows FTIR results for both NPs

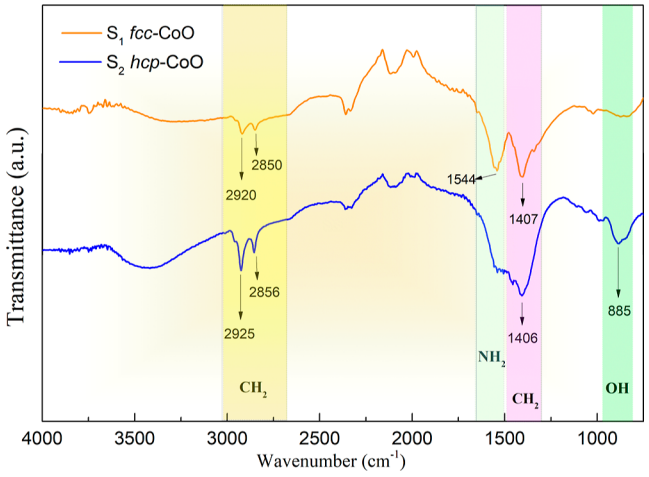

Figure 5. FTIR spectra highlighting the functional groups present in the coating of the nanoparticles, with observed modes NH_2, CH, CH_2, and OH. The spectra for sample S_1 (fcc-CoO) and sample S_2 (hcp-CoO) are represented by the orange and blue solid lines, respectively.

presenting localized bands at 2850 and 2920 cm^{-1}, for sample S_1, and 2856 and 2925 cm^{-1}, for sample S_2. These bands are characteristic of the fatty acid and fatty amine groups. Oleic acid as well as oleylamine present characteristic modes in these groups, with peaks in the 2851−2853 and 2920−2925 cm^{-1} ranges, which are due to the symmetric and asymmetric stretch modes of the CH_2.[37,38] It is difficult to observe other features of the amine group in FTIR measurements because of the superposition of the wide absorption bands of the OH group in the 3200−3500 cm^{-1} range.[39]

The FTIR results for sample S_1 also reveal a vibration band at 1544 cm^{-1}, which is attributed to the distinctive modes of the amine group (scissor mode of NH_2).[37] This mode was not observed for sample S_2 (hcp-CoO) and is associated with oleylamine. The deformation modes of CH in the CH_2 groups[39] are correlated with the absorption bands in the 1400−1470 cm^{-1} range. The bands between 869 and 894 cm^{-1} are indicative of deformation outside the OH plane,[40] and are often present in the carboxylic acids used in the synthesis of the samples. However, the band at 885 cm^{-1} is associated with OH in plane deformation.[40] Our findings are in agreement with the TEM measurements, which indicate that the stability of the organic−inorganic interface dictates the crystallographic growth orientation of the nanoparticles through the dynamic solvation behavior of the surfactants in solution. This interfacial layer potentially offers an additional design parameter for optimizing the nanoparticles for practical applications.

Local Characterization. *Raman Spectroscopy.* At first, both samples were characterized by Raman spectroscopy using a wavelength of 514 nm with laser powers of 12 and 4 mW for samples S_1 (fcc-CoO) and S_2 (hcp-CoO), respectively, with the aim of local analysis. The resulting Raman data were treated by the software Fityk that uses the curve-fitting Levenberg−Marquardt algorithm. The center and shape of the observed bands for the S_1 and S_2 samples were fitted with Lorentzian functions. According to Figure 6a, sample S_1, which was identified by XRD as fcc-CoO, presents Raman spectra with bands at 192, 473, 517, 607, and 683 cm^{-1}. A Raman spectrum with E_g, A_1g, and T_2g vibration modes and Raman shifts of about 489, 540, and 690 cm^{-1} should be expected for the fcc-CoO structure.[13] However, sample S_1 displays distinct bands of Co_3O_4 rather than the typical bands of CoO with fcc structure.

Similarly, sample S_2 exhibited band centers at positions 189, 466, 510, 607, and 678 cm^{-1}. According to theoretical

https://doi.org/10.1021/acsomega.4c05308
ACS Omega 2024, 9, 42883−42894

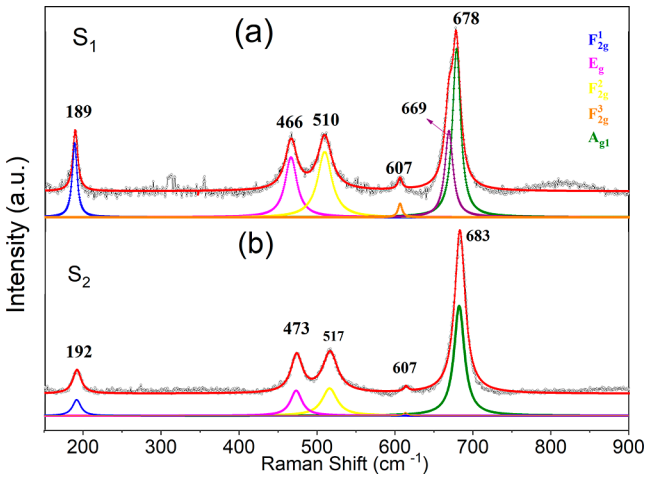

Figure 6. Raman spectra for sample S_1 (fcc-CoO) at 12 mW (a), and for sample S_2 (hcp-CoO) at 4 mW (b). The presented spectra show vibrational modes related to the spinel-type Co_3O_4 phase, suggesting a phase transition induced by the interaction between the laser and the sample.

predictions, the hcp-CoO structure with the space group $P6_3mc$ should display two characteristic bands corresponding to the vibrational modes A_1 (LO) and A_1 (LO + TO) at 565 and 663 cm^{-1}, respectively. However, these bands were not observed in the spectrum of S_2. Instead, the prominent vibrational modes strongly suggest the presence of the cubic spinel structure, belonging to the space group Fd_3m, of Co_3O_4, which it is not evident in the XRD results. In this structure, Co^{2+} ions occupy the tetrahedral sites (8*a*), while Co^{3+} ions occupy the octahedral sites (16*d*).

Therefore, it can be concluded from the Raman spectrum analysis that the bands observed for samples S_1 and S_2 do not correspond to the vibration modes of the fcc-CoO and hcp-CoO phases, respectively. The bands in both spectra are typical of the Co_3O_4 phases. These findings suggest that the interaction of CoO nanoparticles with the light beam of the incident laser, which had a power of 12 mW for S_1 and 4 mW for S_2, respectively, heated the NPs locally to a temperature high enough to induce a phase transition to the spinel structure of the Co_3O_4.

To investigate the local annealing induced by the 514 nm laser, variations in the laser power illumination focused at various parts of the sample were carried out. Samples were placed on slide glass and spread out over a 1 cm^2 area for these measurements. Raman spectra for each sample are shown as a function of laser power in Figure 7. For sample S_1 (fcc-CoO), the Raman spectrum acquired at the lowest laser power (0.06 mW), as shown in Figure 7a, does not exhibit discernible peaks. This indicates that a higher laser power is necessary to generate a measurable Raman signal. When the laser power is increased to 0.21 mW, bands with centers at 193.49, 482.29, and 684.35 cm^{-1} may be observed. The values of 484 and 691 cm^{-1}, reported for the cubic phase of fcc-CoO, attributed to the vibration modes E_g and A_1g[13,17,41] are very similar to the two later values. In contrast, a shift in the band center positions is observed for laser powers greater than 0.70 mW. These values, which are now at 519.34 and 615.41 cm^{-1}, suggest a change from the fcc-CoO structure to the spinel structure of Co_3O_4, indicating the presence of new Raman active modes.

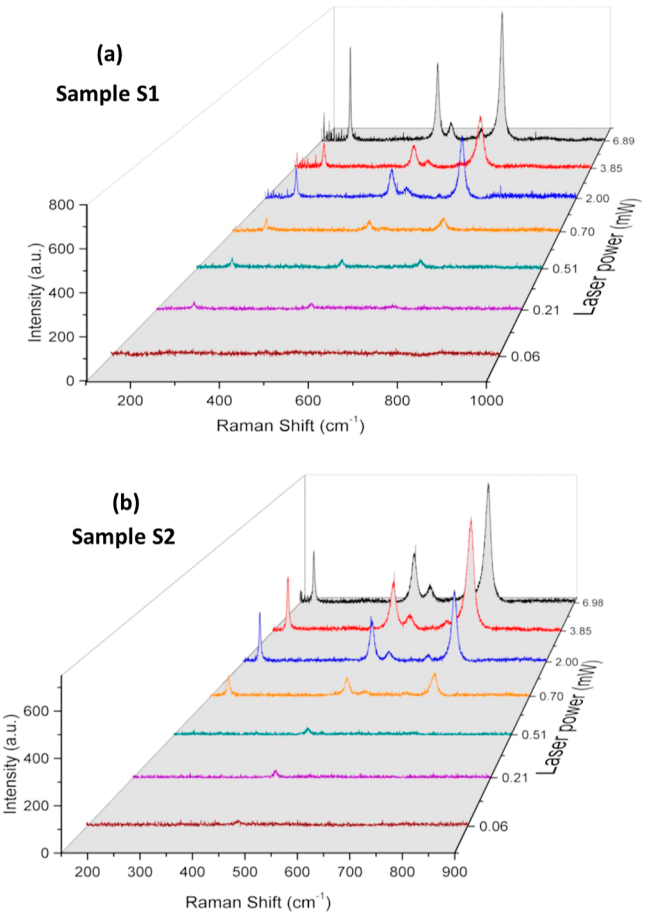

Figure 7. Raman spectra as a function of the laser power to investigate the phase transition by heating induced by the laser incidence on different regions of the CoO nanoparticle samples. (a) Transition from the fcc-CoO to the Co_3O_4 structure for sample S_1. (b) Transition from the wurtzite hcp-CoO to the spinel structure of Co_3O_4 for sample S_2.

The Raman spectrum of Co_3O_4 is evident at 6.89 mW of laser power.

Results of the laser power variation for sample S_2 are shown in Figure 7b. The band centers are located at 448.01, 447.82, and 446.40 cm^{-1}, respectively, for laser powers of 0.06, 0.20, and 0.51 mW. In the hexagonal close-packed hcp-CoO crystal structure, the E_2 phonon mode is observed alongside other vibrational modes. These vibrational modes correspond to band centers located at 447, 565, and 663 cm^{-1} as previously reported.[42,43] Consequently, the characteristic A_1 vibrational mode of hcp-CoO is observed in the Raman spectra acquired at laser power below 0.50 mW. The Raman spectra exhibit a shift when the laser power is increased to 0.70 mW or higher above. These spectra now show band centers at 191.83, 471.75, 511.57, 610.81, and 679.24 cm^{-1}, suggesting a full transition to the Co_3O_4 phase.

Raman spectroscopy measurements as a function of laser power suggest a local phase transformation in both samples S_1 and S_2 to the Co_3O_4 structure, with nanoparticles localized in regions exposed to laser irradiation. This phenomenon is triggered by the highly concentrated energy of the laser beam, which raises the temperature of nanoparticles, provoking a change in their crystalline structure. This process is usually referred to as "laser-induced phase transition" and has diverse

https://doi.org/10.1021/acsomega.4c05308
ACS Omega 2024, 9, 42883−42894

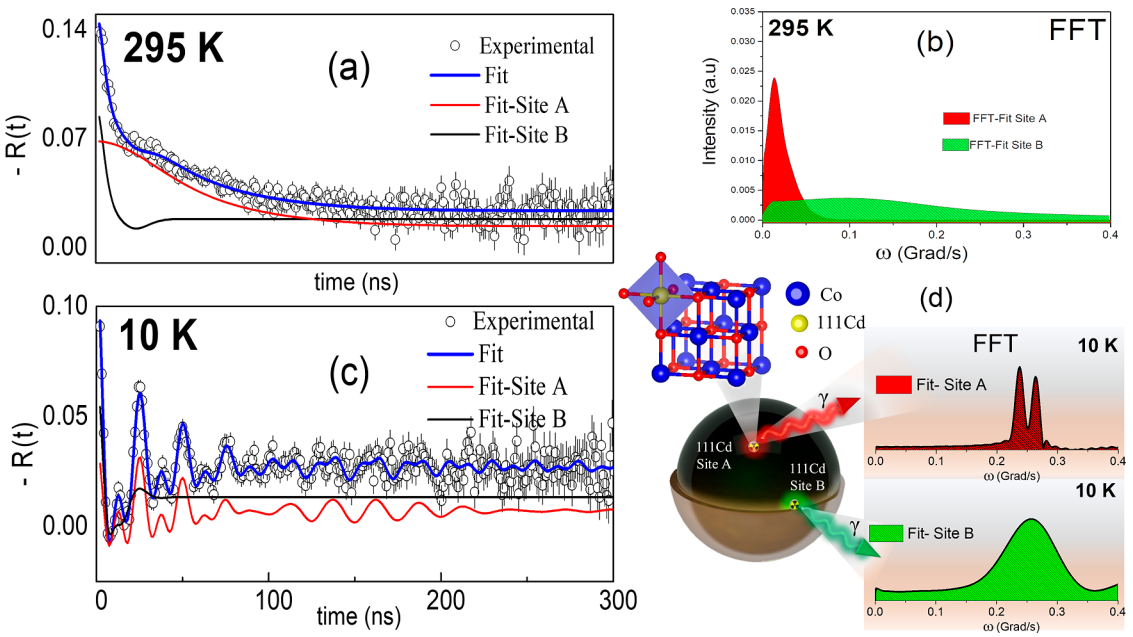

Figure 8. PAC measurements for S_1. (a) Time-differential anisotropy ratio function $R(t)$ and (b) the fast Fourier transform (FFT) at room temperature fitted with a two-site model: site A (red) with a pure electric interaction and site B (green) with a broad distributed electric interaction. (c) $R(t)$ function and (d) its respective fast Fourier transform (FFT) at 10K fitted with a two-site model considering combined electric plus magnetic interactions.

Table 1. Hyperfine Interaction Parameters of Sample S_1 Nanoparticles using a Two-Site model—Site a in the NPs' Core and Site B in Their Outer layer—at Room Temperature (295 K) and 10 K

site	$T(K)$	$f(\%)$	ν_Q(MHz)	ν_M(MHz)	η	$\delta(\%)$
A	295	40.0 ± 1.0	11.0 ± 0.5	0.0 ± 0.0	0.0	52.0 ± 7.0
B	295	60.0 ± 1.0	64.0 ± 7.0	0.0 ± 0.0	0.7	83.0 ± 9.0
A	10	37.0 ± 1.0	8.0 ± 0.5	40.2 ± 0.1	0.0	1.0 ± 0.1
B	10	63.0 ± 1.0	17.0 ± 0.5	42.4 ± 0.7	0.0	15.0 ± 2.0

applications, including nanofabrication and the study of nanoparticle properties.

It is crucial to emphasize that the laser wavelength, its power density, and the irradiation time, along with the intrinsic properties of the nanoparticles, are critical factors governing the induction of the desired phase. This approach offers significant advantages for the controlled modulation of nanoparticle properties, enabling the emergence of novel phenomena at the nanometric scale.

Perturbed Angular Correlations. PAC measurements on fcc-CoO (S_1) and hcp-CoO (S_2) were carried out using ^{111}In(^{111}Cd) as probe nucleus at room temperature (RT) and at 10 K, respectively. For S_1, the time-dependent anisotropy ratio function, $R(t)$, and their respective fast Fourier transforms, resulting from PAC measurements, are represented in Figure 8. The hyperfine parameters used to fit the $R(t)$ spectra in Figure 8 are recorded in Table 1, considering a two-site fitting model, namely, site A and site B.

At RT, a symmetric ($\eta = 0$) quadrupole interaction was found to represent site A that is characterized by a low quadrupole frequency ν_{QA} = 11 MHz with a very broad distribution δ_A = 52% and a site fraction of f_A = 40%. This low quadrupolar interaction corresponds to the probe nucleus substituting a cation position in the crystalline structure (see the continuous red line fit). Site B, on the other hand, presents a higher fractional population (f_B = 60%), characterized by a wide frequency distribution (δ_A = 83%) and a $\nu_{QB} \sim 64$ MHz (see the continuous green line fit), which was attributed to the probe nuclei occupying the outer layer of nanoparticles rich in residual organic material.

For the PAC measurements on S_1 at 10 K, the $R(t)$ spectrum shown in Figure 8c, exhibits characteristic oscillations due to the transferred magnetic hyperfine field (B_{hf}) interaction with a well-defined frequency (δ_A = 1%), as seen in the FFT spectrum (see Figure 8d). The fitting was performed with a two-site fraction model, where site A has a population f_A = 37%, with $\nu_{QA} \sim 8$ MHz and Larmor frequency ν_M = 40.2 MHz, equivalent to B_{hf} = 17 T. This site shows a low-frequency distribution attributed to the substitutional position of the probe nucleus. Site B has f_B = 63% with δ_A = 15%. This fractional population has been assigned to the probe nuclei in the outer layer of the particles. At this site, ν_{QB} = 17 MHz and ν_M = 42.4 MHz, which is equivalent to B_{hf} = 18 T. The data are consistent with the systematic work published by Santos et al. on CoO, bulk, and NPs.[25] At the external regions of the NPs, low symmetry and crystallinity are attributed to the amorphous formation of the organic material coating the NPs. It is important to mention that coating or encapsulation plays an important role in the stability and functionality of nanoparticles.

The time-dependent anisotropy ratio function $R(t)$ of sample S_2 at room temperature displayed pronounced damping. The hyperfine parameters used for the fit of the $R(t)$ spectra in Figure 9 were recorded in Table 2, considering

https://doi.org/10.1021/acsomega.4c05308
ACS Omega 2024, 9, 42883−42894

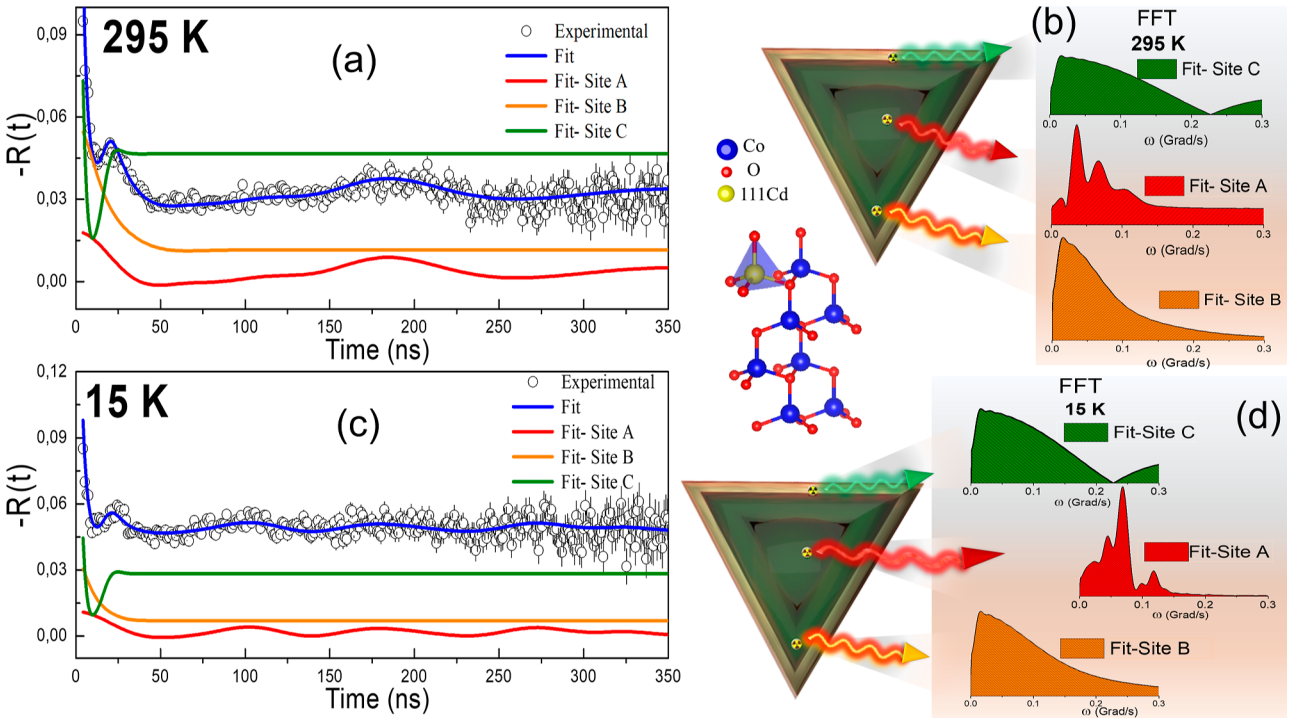

Figure 9. PAC measurements for S_2 (a) time-differential anisotropy ratio function $R(t)$, and (b) the fast Fourier transform (FFT) at room temperature fitted with a three-site model considering pure electric quadrupole interactions: site A (red), and site B (orange) and site C (green), both with broad frequency distributions. (c) Time-differential anisotropy ratio function $R(t)$ and (d) its corresponding fast Fourier transform (FFT) at 15 K fitted with a three-site model considering for site A a combined electric plus magnetic interactions, and for sites B and C pure electric quadrupole interactions.

Table 2. Hyperfine Interaction Parameters of Sample S_2 Nanoparticles at Room Temperature (295 K) and 15 K using a Three-Site Model: Site a Inside the NPs, Site B Surface the NPs, and Site C Outside Region

site	$T(K)$	$f(\%)$	ν_Q(MHz)	ν_M(MHz)	η	$\delta(\%)$
A	295	17.0 ± 1.0	33.0 ± 0.4	0.0	0.3	10.0 ± 1.2
B	295	17.0 ± 1.0	29.0 ± 0.6	0.0	0.0	33.0 ± 4.5
C	295	66.0 ± 1.0	207.0 ± 9.51	0.0	0.3	60.0 ± 7.0
A	15	15.0 ± 1.0	33.0 ± 0.7	2.5 ± 0.2	0.3	5.0 ± 0.2
B	15	15.0 ± 1.0	29.0 ± 0.6	0.0	0.3	40.0 ± 8.0
C	15	70.0 ± 1.0	207.0 ± 0.8	0.0	0.5	31.0 ± 3.0

a model of three-site fitting, site A, site B and site C, which reveals valuable information about the local structure (see Figure 9a). Site A (red line) can be interpreted as the occupation of the probe nucleus, ^{111}In(^{111}Cd), in crystalline substitutional sites in pyramidal or hexagonal sample nanoparticles, as it showed a δ = 10% (Figure 9b). This high crystallinity phase was identified in the internal regions of the NPs, as shown in the TEM images in Figure 4e. The electric quadrupolar frequency extracted from the $R(t)$ spectrum was ν_{QA} ~33 MHz, and this value matches the value reported in Pereira et al. for the impurities ^{111} Cd located at defect-free cation sites in the codoped ZnO structure (whose value is ν_{QA} ~33 MHz).[44] In addition, taking into account the Co solubility threshold in ZnO, a stable physical situation occurs in this region: with an increase in Co doping concentration in the ZnO host matrix, the system exhibits a solution-like behavior, favoring the formation of diluted clusters and the consolidation of metastable phases such as a ZnO−CoO. In other words, the CoO clusters in Pereira et al., have the same space group ($P6_3mc$) and point group ($6mm$) of the hcp-CoO sample S_2 nanoparticles (see Figure 9a), justifying the similar hyperfine parameters obtained from both studies. This is seen more clearly in the correspondent band structure calculations,[44] where the Cd and Co impurity bands are fully hybridized with the band characteristic of the ZnO host matrix (bands coexisting at the same energy level).

At 15 K, the sample S_2, hcp-CoO nanoparticles, exhibit relatively low magnetic interaction associated with weak magnetic coupling. A combined interaction model (electric quadrupolar plus magnetic dipolar interactions) was used to fit site A at 15 K, which produced a magnetic Larmor frequency, ν_M = 2.5 MHz, equivalent to a transferred hyperfine field of B_{hf} = 0.86 T, significantly lower than B_{hf} of the fcc-CoO phase, which was B_{hf} ~ 17 T at 10 K. This aspect (low hyperfine field), reinforces the hypothesis of weak magnetic coupling in this system, as suggested by several authors through electron spin resonance (ESR) spectroscopy measurements.[17,45]

Site B (orange line) has been identified as probe nuclei located in a region close to the surface of the NPs, characterized by bond breaks and low crystallinity. The low crystallinity at RT was confirmed by the observation of ν_{QB} = 29.0(1) MHz with a broad frequency distribution (δ = 33%) at

https://doi.org/10.1021/acsomega.4c05308
ACS Omega 2024, 9, 42883−42894

this site. Furthermore, no transferred hyperfine field was seen at low temperatures, such as 15 K, because of the weak magnetic coupling in the hcp-CoO system, which is susceptible to symmetry breaks and defects that are typical of the surface region in these NPs.

At site C (green line), there is a high fractional population (f_C = 66%) with a high electrical frequency value (ν_{QC} ≈207 MHz), with η = 0.3, and δ = 60%. This broad frequency distribution characterizes probe nuclei in the outer region of the nanoparticles, which are made up of residual amorphous organic material. The presence of organic material surrounding the nanoparticles was confirmed by FTIR measurements and TEM images, as shown in Figures 5 and 4c,d, respectively.

Finally, the analysis of substitutional sites in samples S_1 and S_2 at low-temperature measurements revealed a weak transferred hyperfine field (B_{hf}) for ^{111}In(^{111}Cd) in the hcp-CoO crystal lattice (S_2), which was approximately B_{hf} = 1 T. This value is significantly lower than that observed in the fcc-CoO phase (S_1), which was around 17 T. The superexchange interaction, in which the spin density is transferred from the paramagnetic Co ions to the diamagnetic Cd ions via O ions (through the Co−O−Cd bonds), is the cause of the weakening of the hyperfine magnetic field at the Cd probes in hcp-CoO. This transfer takes place through the spin polarization of the closed s shells of Cd by magnetic neighbors through the overlap of the oxygen p orbital, transferring unpaired spin density into the outermost Cd 5s orbital.[46]

Since orbitals with rotational symmetry around the bond axis (e_g orbitals: d_z^2 and $d_{x^2-y^2}$) transfer maximum spin density, these should be considered in the first place. If e_g orbitals are empty, the t_2g orbitals (d_{xy}, d_{yz}, d_{zx}), which have relatively small overlap with the orbitals of nearby oxygen ions, transfer less spin density to Cd orbitals via Co−O−Cd exchange bonds. As a consequence, the supertransferred magnetic hyperfine field at ^{111}Cd nuclei would be smaller for Co−O−Cd bond angles closer to 90° than those closer to 180°.

Therefore, the origin of the big difference in B_{hf} is essentially due to the different geometries in both systems. The hcp-CoO structure has a hexagonal geometry, with a complex magnetic structure that induces spin frustration, weakening the superexchange mechanism through Co^{2+}−O^{2-}−Co^{2+} bonds due to the characteristic angle of 110°, also known as two-dimensional frustration.[17,47−49] However, the superexchange interaction is stronger in the rock-salt structure, featuring an antiferromagnetic type II (AFM-II) magnetic structure, favored by linear superexchange between Co^{2+}−O^{2-}−Co^{2+} bonds with an angle of 180°.[50,51] Additionally, it is also suggested that the magnetism in hcp-CoO is possibly dependent on the morphology and type of defects in its structure (e.g., oxygen vacancies, stacking faults, among others, provided by synthesis procedure), which may contribute to different manifestations of magnetic behaviors.

CONCLUSIONS

Samples of CoO nanoparticles were synthesized with the thermal decomposition method using two different ligand pairs: one sample with the oleylamine/oleic acid ligand pair, and the other with only oleylamine. Data analysis of X-ray patterns revealed characteristic patterns of the unique phases for each sample after synthesis, rock-salt cubic fcc phase with an average size of 5 nm, and wurtzite hexagonal hcp phase with a size of 43 nm, respectively.

Raman spectra analysis indicated similarities in bands for both samples, suggesting a localized phase transformation process induced by laser-power density, resulting in the formation of the Co_3O_4. The measurements reveal that the surfaces of both fcc-CoO and hcp-CoO NPs are susceptible and unstable under incident light power, which may influence the properties of the NPs triggering a local crystalline phase transition to Co_3O_4 as observed.

PAC measurements for doped samples, with probe nuclei ^{111}In(^{111}Cd), during the synthesis process, revealed weaker transferred hyperfine fields in the hcp-CoO phase (B_{hf} = 1 T) compared to the fcc-CoO phase (B_{hf} = 17 T), indicating that superexchange interactions are strongly influenced by the angle 110° for hcp-CoO and an angle 180° for fcc-CoO due to the system geometries. Both Raman and PAC measurements show low crystallinity on the surfaces of the NPs, as revealed by the low intensity of the Raman bands at low powers and the high damping (δ) of the $R(t)$ spectra. The complementary techniques provide valuable insights into the crystalline and magnetic properties of CoO polymorphs.

AUTHOR INFORMATION

Corresponding Authors

Artur W. Carbonari − *Instituto de Pesquisas Energéticas e Nucleares IPEN-CNEN/SP, São Paulo, São Paulo 05508-000, Brazil; EP Department, European Organization for Nuclear Research (CERN), Geneva CH-1211, Switzerland;* orcid.org/0000-0002-4499-5949; Email: carbonar@ipen.br

Gabriel A. Cabrera-Pasca − *Faculdade de Ciências Exatas e Tecnologia, Universidade Federal do Pará (UFPA), Abaetetuba, Pará 684440-000, Brazil*; Email: gpasca@ufpa.br

Authors

Suzilene V. Santos − *Programa de Pós-Graduação em Ciência e Engenharia de Materiais − PPGCEM, Universidade Federal do Pará (UFPA), Ananindeua, Pará 67130-660, Brazil*

Cleidilane S. Costa − *Faculdade de Ciências Exatas e Tecnologia, Universidade Federal do Pará (UFPA), Abaetetuba, Pará 684440-000, Brazil*

Waldeci Paraguassu − *Programa de Pós-Graduação em Ciência e Engenharia de Materiais − PPGCEM, Universidade Federal do Pará (UFPA), Ananindeua, Pará 67130-660, Brazil*

Crystian W. C. Silva − *Instituto de Pesquisas Energéticas e Nucleares IPEN-CNEN/SP, São Paulo, São Paulo 05508-000, Brazil*

Larissa Otubo − *Instituto de Pesquisas Energéticas e Nucleares IPEN-CNEN/SP, São Paulo, São Paulo 05508-000, Brazil*

Katiusse S. Souza − *Instituto de Pesquisas Energéticas e Nucleares IPEN-CNEN/SP, São Paulo, São Paulo 05508-000, Brazil*

Bruno S. Correa − *Instituto de Pesquisas Energéticas e Nucleares IPEN-CNEN/SP, São Paulo, São Paulo 05508-000, Brazil*

Arnaldo A. Miranda-Filho − *Instituto de Pesquisas Energéticas e Nucleares IPEN-CNEN/SP, São Paulo, São Paulo 05508-000, Brazil*

Wanderson L. Ferreira − *Instituto de Pesquisas Energéticas e Nucleares IPEN-CNEN/SP, São Paulo, São Paulo 05508-000, Brazil*

https://doi.org/10.1021/acsomega.4c05308
ACS Omega 2024, 9, 42883−42894

Complete contact information is available at:
https://pubs.acs.org/10.1021/acsomega.4c05308

Funding

The Article Processing Charge for the publication of this research was funded by the Coordination for the Improvement of Higher Education Personnel - CAPES (ROR identifier: 00x0ma614).

Notes

The authors declare no competing financial interest.

■ ACKNOWLEDGMENTS

A.W. Carbonari acknowledges the financial support received from Conselho Nacional de Desenvolvimento Científico e Tecnológico (CNPq) and Fundação de Amparo a Pesquisa do Estado de São Paulo (FAPESP) under grants 304627/2017-8 and grants 2014/14001-1 and 2017/50332-0, respectively, as well as from the Instituto de Pesquisas Energéticas e Nucleares IPEN-CNEN/SP for financial support under projects 2020.06.IPEN.43 and 2020.06.IPEN.38. G.A. Cabrera-Pasca gratefully acknowledges support of the RCGI—Research Centre for Greenhouse Gas Innovation, hosted by the University of São Paulo (USP) and sponsored by FAPESP—São Paulo Research Foundation (2014/50279-4 and 2020/15230-5) and Shell Brasil, and the strategic importance of the support given by ANP (Brazil's National Oil, Natural Gas and Biofuels Agency) through the R&D levy regulation. B.S. Correa thanks the Conselho Nacional de Desenvolvimento Científico e Tecnológico (CNPq) for financial support through grant numbers 142070/2019-0. A. A.A.M.-F. and W. L. Ferreira acknowledges the Coordenação de Aperfeiçoamento de Pessoal de Nível Superior (CAPES) for financial support through grant numbers 88887.661225/2022-00 and 88887.513796/2020-00, respectively. The authors acknowledge the use of the facilities and the technical assistance of the Laboratório de Espectroscopia Vibracional e Altas Pressões (LEVAP), hosted by the Federal University of Pará (UFPA). This will usually read something like: Experimental procedures and characterization data for all new compounds. The class will automatically add a sentence pointing to the information online.

■ REFERENCES

(1) Altammar, K. A. A review on nanoparticles: characteristics, synthesis, applications, and challenges. *Front. Microbiol.* **2023**, *14*, 1155622.
(2) Willard, M.; Kurihara, L.; Carpenter, E.; Calvin, S.; Harris, V. Chemically prepared magnetic nanoparticles. *Int. Mater. Rev.* **2004**, *49*, 125−170.
(3) Haleem, A.; Javaid, M.; Singh, R. P.; Rab, S.; Suman, R. Applications of nanotechnology in medical field: a brief review. *J. Glob. Health* **2023**, *7*, 70−77.
(4) Issa, B.; Obaidat, I.; Albiss, B.; Haik, Y. Magnetic Nanoparticles: Surface Effects and Properties Related to Biomedicine Applications. *Int. J. Mol. Sci.* **2013**, *14*, 21266−21305.
(5) Ho, C.-H.; Lai, C.-H. Size-Dependent Magnetic Properties of PtMn Nanoparticles. *IEEE Trans. Magn.* **2006**, *42*, 3069−3071.
(6) Frenkel, A. I.; Hills, C. W.; Nuzzo, R. G. A view from the inside: Complexity in the atomic scale ordering of supported metal nanoparticles. *J. Phys. Chem. B* **2001**, *105*, 12689−12703.
(7) Vayssières, L.; Chanéac, C.; Tronc, E.; Jolivet, J. P. Size Tailoring of Magnetite Particles Formed by Aqueous Precipitation: An Example of Thermodynamic Stability of Nanometric Oxide Particles. *J. Colloid Interface Sci.* **1998**, *205*, 205−212.
(8) Etacheri, V.; Hong, C. N.; Tang, J.; Pol, V. G. Cobalt Nanoparticles Chemically Bonded to Porous Carbon Nanosheets: A Stable High-Capacity Anode for Fast-Charging Lithium-Ion Batteries. *ACS Appl. Mater. Interfaces* **2018**, *10*, 4652−4661.
(9) Dey, S.; Dhal, G. The catalytic activity of cobalt nanoparticles for low-temperature oxidation of carbon monoxide. *Mater. Today Chem.* **2019**, *14*, 100198.
(10) Li, W.; Jung, H.; Hoa, N. D.; Kim, D.; Hong, S.-K.; Kim, H. Nanocomposite of cobalt oxide nanocrystals and single-walled carbon nanotubes for a gas sensor application. *Sens. Actuators, B* **2010**, *150*, 160−166.
(11) Ansari, S.; Bhor, R.; Pai, K.; Sen, D.; Mazumder, S.; Ghosh, K.; Kolekar, Y.; Ramana, C. Cobalt nanoparticles for biomedical applications: Facile synthesis, physiochemical characterization, cytotoxicity behavior and biocompatibility. *Appl. Surf. Sci.* **2017**, *414*, 171−187.
(12) Song, Y.; Modrow, H.; Henry, L. L.; Saw, C. K.; Doomes, E. E.; Palshin, V.; Hormes, J.; Kumar, C. S. S. R. Microfluidic Synthesis of Cobalt Nanoparticles. *Chem. Mater.* **2006**, *18*, 2817−2827.
(13) Ravindra, A. V.; Behera, B. C.; Padhan, P. Laser Induced Structural Phase Transformation of Cobalt Oxides Nanostructures. *J. Nanosci. Nanotechnol.* **2014**, *14*, 5591−5595.
(14) Macheli, L.; Leteba, G. M.; Doyle, B. P.; Jewell, L.; van Steen, E. Modulating CO hydrogenation activity through silane functionalization of cobalt catalysts. *Applied Appl. Catal. A: Gen.* **2024**, *685*, 119874.
(15) Cai, Y.; Xu, J.; Guo, Y.; Liu, J. Ultrathin, Polycrystalline, Two-Dimensional Co_3O_4 for Low-Temperature CO Oxidation. *ACS Catal.* **2019**, *9*, 2558−2567.
(16) Karadaghi, L. R.; Williamson, E. M.; To, A. T.; Forsberg, A. P.; Crans, K. D.; Perkins, C. L.; Hayden, S. C.; LiBretto, N. J.; Baddour, F. G.; Ruddy, D. A.; Malmstadt, N.; Habas, S. E.; Brutchey, R. L. Multivariate Bayesian Optimization of CoO Nanoparticles for CO_2 Hydrogenation Catalysis. *J. Am. Chem. Soc.* **2024**, *146*, 14246−14259.
(17) He, X.; Song, X.; Qiao, W.; Li, Z.; Zhang, X.; Yan, S.; Zhong, W.; Du, Y. Phase- and Size-Dependent Optical and Magnetic Properties of CoO Nanoparticles. *J. Phys. Chem. C* **2015**, *119*, 9550−9559.
(18) He, X.; Zhong, W.; Yan, S.; Liu, C.; Shi, H.; Au, C.-T.; Du, Y. Transition Temperature of Wurtzite CoO Nanocrystals as Revealed in Comprehensive Magnetic Characterization. *J. Phys. Chem. C* **2014**, *118*, 13898−13903.
(19) Deori, K.; Deka, S. Morphology oriented surfactant dependent CoO and reaction time dependent Co_3O_4 nanocrystals from single synthesis method and their optical and magnetic properties. *CrystEngComm* **2013**, *15*, 8465.
(20) Baer, D. R.; Engelhard, M. H.; Johnson, G. E.; Laskin, J.; Lai, J.; Mueller, K.; Munusamy, P.; Thevuthasan, S.; Wang, H.; Washton, N.; Elder, A.; Baisch, B. L.; Karakoti, A.; Kuchibhatla, S. V. N. T.; Moon, D. Surface characterization of nanomaterials and nanoparticles: Important needs and challenging opportunities. *J. Vac. Sci. Technol. A: Vac. Surf. Films.* **2013**, *31*, 50820.
(21) Corrêa, B. S.; Costa, M. S.; Cabrera-Pasca, G. A.; Sena, C.; Holanda Pinto, R. H.; Silva, A. P. S.; Carvalho Junior, R. N.; Ishida, L.; Ramon, J. G. A.; Freitas, R. S.; Saiki, M.; Matos, I. T.; Correa, E. L.; Carbonari, A. W. High-saturation magnetization in small nanoparticles of Fe_3O_4 coated with natural oils. *J. Nanopart. Res.* **2020**, *22*, 68.
(22) Campos, A. C.; Paes, S. C.; Correa, B. S.; Cabrera-Pasca, G. A.; Costa, M. S.; Costa, C. S.; Otubo, L.; Carbonari, A. W. Growth of Long ZnO Nanowires with High Density on the ZnO Surface for Gas Sensors. *ACS Appl. Nano Mater.* **2020**, *3*, 175−185.
(23) Carbonari, A. W.; Mestnik-Filho, J.; Saxena, R. N. Impurities in Magnetic Materials Studied by PAC Spectroscopy. *Defect Diffus. Forum* **2011**, *311*, 39−61.
(24) Silva, C. W. C.; Cabrera-Pasca, G. A.; Souza, K. S.; Costa, C. S.; Costa, M. S.; Correa, B. S.; Ferreira, W. L.; Freitas, R. S.; Carbonari, A. W.; Otubo, L. Investigation of Ni/Ni3C Nanoparticle Synthesis for

Application as a Catalyst in Carbon Nanostructure Growth. *ACS Appl. Nano Mater.* **2023**, *6*, 20623−20638.
(25) Santos, R. V.; Cabrera-Pasca, G. A.; Costa, C. S.; Bosch-Santos, B.; Otubo, L.; Pereira, L. F. D.; Correa, B. S.; Effenberger, F. B.; Burimova, A.; Freitas, R. S.; Carbonari, A. W. Crystalline and magnetic properties of CoO nanoparticles locally investigated by using radioactive indium tracer. *Sci. Rep.* **2021**, *11*, 21028.
(26) Mokhles Gerami, A.; Heiniger-Schell, J.; da Silva, E. L.; Costa, M. S.; Costa, C. S.; Monteiro, J. G.; Pires, J. J.; Pereira, D. R.; Díaz-Guerra, C.; Carbonari, A. W.; Lorenz, K.; Correia, J. G.; Correia, J. G. Cd implantation αMoO_3: An atomic scale study. *Phys. Rev. Mater.* **2023**, *7*, 033603.
(27) Frauenfelder, H.; Steffen, R. Alpha-, beta-, and gamma-ray spectroscopy. *Angular Correl.* **1965**, *997*, 275−276.
(28) Carbonari, A. W.; Jr, W. P.; Attili, R.; Saxena, R. N. Magnetic hyperfine fields in the Heusler alloys Co_2YZ (Y = Sc, Ti, Hf, V, Nb; Z = A1, Ga, Si, Ge, Sn). *Hyperfine Interact.* **1993**, *80*, 971−976.
(29) Lyu, S.; Wang, S.; He, Z.; Yang, J.; Xu, X.; Carabineiro, S. A.; Zhu, J. Lattice Matching Strategy to Construct Highly Active hcp-Co Phase for Fischer−Tropsch Synthesis. *ACS Mater. Lett.* **2024**, *6*, 856−864.
(30) Shirsath, S. E.; Liu, X.; Yasukawa, Y.; Li, S.; Morisako, A. Switching of magnetic easy-axis using crystal orientation for large perpendicular coercivity in $CoFe_2O_4$ thin film. *Sci. Rep.* **2016**, *6*, 30074.
(31) Pham, C. D.; Chang, J.; Zurbuchen, M. A.; Chang, J. P. Magnetic Properties of $CoFe_2O_4$ Thin Films Synthesized by Radical-Enhanced Atomic Layer Deposition. *ACS Appl. Mater. Interfaces* **2017**, *9*, 36980−36988.
(32) Tracy, J. B.; Bawendi, M. G. Defects in CoO in oxidized cobalt nanoparticles dominate exchange biasing and exhibit anomalous magnetic properties. *Phys. Rev. B* **2006**, *74*, 184434.
(33) Sharma, V.; Verma, D.; Okram, G. S.; Choudhary, R. J.; Kumar, D.; Deshpande, U. Dominant role of trioctylphosphine on the particle size and various properties of CoO nanoparticles. *J. Magn. Magn. Mater.* **2020**, *497*, 166000.
(34) Jang, K. Y.; Ahn, S. J.; Kwon, J.-H.; Nam, K. M.; Kim, Y. H. Novel Route from a Wurtzite to a Rock-Salt Structure in CoO Nanocrystals: In Situ Transmission Electron Microscopy Study. *J. Phys. Chem. C* **2019**, *123*, 10689−10694.
(35) Nam, K. M.; Shim, J. H.; Han, D. W.; Kwon, H. S.; Kang, Y. M.; Li, Y.; Song, H.; Seo, W. S.; Park, J. T. Syntheses and characterization of wurtzite CoO, rocksalt CoO, and spinel Co_3O_4 nanocrystals: their interconversion and tuning of phase and morphology. *Chem. Mater.* **2010**, *22*, 4446−4454.
(36) Kong, F.-C.; Li, Y.-F.; Shang, C.; Liu, Z.-P. Stability and phase transition of cobalt oxide phases by machine learning global potential energy surface. *J. Phys. Chem. C* **2019**, *123*, 17539−17547.
(37) Berti, I. O. P. D.; Cagnoli, M. V.; Pecchi, G.; Alessandrini, J. L.; Stewart, S. J.; Bengoa, J. F.; Marchetti, S. G. Alternative low-cost approach to the synthesis of magnetic iron oxide nanoparticles by thermal decomposition of organic precursors. *Nanotechnolgy* **2013**, *24*, 175601.
(38) Betancourt-Galindo, R.; Reyes-Rodriguez, P. Y.; Puente-Urbina, B. A.; Avila-Orta, C. A.; Rodríguez-Fernández, O. S.; Cadenas-Pliego, G.; Lira-Saldivar, R. H.; García-Cerda, L. A. Synthesis of copper nanoparticles by thermal decomposition and their antimicrobial properties. *J. Nanomaterials* **2014**, *2014*, 980545.
(39) Safo, I. A.; Dosche, C.; Özaslan, M. Effects of capping agents on the oxygen reduction reaction activity and shape stability of Pt nanocubes. *ChemPhysChem* **2019**, *20*, 3010−3023.
(40) Jahangirian, H.; Haron, M. J.; Yusof, N. A.; Silong, S.; Kassim, A.; Rafiee-Moghaddam, R.; Peyda, M.; Gharayebi, Y. Enzymatic synthesis of fatty hydroxamic acid derivatives based on palm kernel oil. *Molecules* **2011**, *16*, 6634−6644.
(41) Gallant, D.; Pezolet, M.; Simard, S. Optical and physical properties of cobalt oxide films electrogenerated in bicarbonate aqueous media. *J. Phys. Chem. C* **2006**, *110*, 6871−6880.
(42) Rivas-Murias, B.; Salgueiriño, V. Thermodynamic CoO−Co_3O_4 crossover using Raman spectroscopy in magnetic octahedron-shaped nanocrystals. *J. Raman Spectroscopy* **2017**, *48*, 837−841.
(43) Choi, H. C.; Jung, Y. M.; Kim, S. B. Size effects in the Raman spectra of TiO_2 nanoparticles. *Vib. Spectrosc.* **2005**, *37*, 33−38.
(44) Pereira, L. F.; Ferreira, W. L.; Correa, B. S.; Costa, M. S.; Costa, C. S.; Filho, A. A.; Sales, T. S.; Bosch-Santos, B.; Schell, J.; Burimova, A.; et al. Cobalt Doping Effects in Zinc Oxide: A Combined Experimental and Ab Initio Approach. *Crystals* **2023**, *14*, 51.
(45) He, X.; Shi, H. Synthesis and anomalous magnetic properties of hexagonal CoO nanoparticles. *Mater. Res. Bull.* **2011**, *46*, 1692−1697.
(46) Dogra, R.; Junqueira, A. C.; Saxena, R. N.; Carbonari, A. W.; Mestnik-Filho, J.; Moralles, M. Hyperfine interaction measurements in $LaCrO_3$ and $LaFeO_3$ perovskites using perturbed angular correlation spectroscopy. *Phys. Rev. B* **2001**, *63*, 224104.
(47) Roca, A. G.; Golosovsky, I. V.; Winkler, E.; López-Ortega, A.; Estrader, M.; Zysler, R. D.; Baró, M. D.; Nogués, J. Unravelling the Elusive Antiferromagnetic Order in Wurtzite and Zinc Blende CoO Polymorph Nanoparticles. *Small* **2018**, *14*, 1703963.
(48) Alaria, J.; Cheval, N.; Rode, K.; Venkatesan, M.; Coey, J. M. D. Structural and magnetic properties of wurtzite CoO thin films. *J. Phys. D: Appl. Phys.* **2008**, *41*, 135004.
(49) Archer, T.; Hanafin, R.; Sanvito, S. Magnetism of CoO polymorphs: Density functional theory and Monte Carlo simulations. *Phys. Rev. B* **2008**, *78*, 014431.
(50) Jauch, W.; Reehuis, M.; Bleif, H. J.; Kubanek, F.; Pattison, P. Crystallographic symmetry and magnetic structure of CoO. *Phys. Rev. B* **2001**, *64*, 052102.
(51) Qi, Q.; Chen, Y.; Wang, L.; Zeng, D.; Peng, D.-L. Phase-controlled synthesis and magnetic properties of cubic and hexagonal CoO nanocrystals. *Nanotechnology* **2016**, *27*, 455602.

https://doi.org/10.1021/acsomega.4c05308
ACS Omega 2024, 9, 42883−42894